

Physics-Based Approaches for Sizing Thermal Management Systems for Battery-Electric Regional Aircraft

Sai Sankalp Shekar* and Matthew A. Clarke†
University of Illinois, Urbana-Champaign, Urbana, Illinois, 61801

Dissipating the waste heat produced by electrical losses is pertinent for achieving optimal performance of electromechanical systems, particularly for electric aircraft that operate at megawatt power levels. This paper presents a comprehensive design methodology for battery thermal management systems (BTMS) tailored to the unique demands of electric aircraft. The approach utilizes physics-based modeling to size the heat acquisition system, heat exchanger system, and auxiliary components. For the heat acquisition system, a conjugate cooling strategy is deployed within each battery pack module to extract heat efficiently. This heat is then ejected into the atmosphere via a fuselage-integrated heat exchanger. This study aims to quantify the power requirements of individual components of the BTMS across the different flight stages. Moreover, by determining the upper bounds of the achievable range for this 19-seater aircraft, which stands among the largest vehicles that fall under the Title 14 Code of Federal Regulations Part 23 jurisdiction, we are able to provide realistic estimates of regional air mobility within metropolitan areas. This study enables exploration into BTMS controller design to optimize its utilization to prolong battery life during nominal flight operations, as well as demonstrate safe thermal management during emergency engine failure scenarios. It therefore marks a pivotal stride in the ongoing advancement of thermal management systems tailored for the unique challenges posed by electric aviation.

Nomenclature

A	= Surface area	V	= Voltage
A_o	= Minimum free flow area of HEX	v	= Velocity
c_p	= Specific heat capacity	ΔP	= Pressure difference
C_{rat}	= C-rating	ε	= Effectiveness
D	= Diameter	ρ	= Density
d_h	= Hydraulic diameter	σ	= Ratio of Minimum free-flow area to the frontal area of HEX
E	= Energy	η	= Efficiency
G	= Core mass velocity		
H	= Height		
I	= Current		
j_f	= Ratio of Colburn factor to friction factor		
L	= Length		
m	= Mass		
\dot{m}	= Mass flow rate		
N	= Number of []		
NTU	= Number of Transfer Units		
P	= Power		
r	= Radius		
R	= Resistance		
SOC	= State of Charge		
T	= Temperature		

Subscripts	
bat	= Battery
c	= Cold fluid (air)
$chan$	= Wavy channel of HAS
f	= Fin of HEX
h	= Hot fluid (coolant)
HEX	= Heat exchanger system
HAS	= Heat acquisition system
i	= Inlet
o	= Outlet
0	= Overall

*Graduate Research Assistant and AIAA Student Member

†Assistant Professor and AIAA Professional Member.

I. Introduction

WITH several advantages over fossil-fuel-burning engines, battery-powered electrified flight is expected to revolutionize aviation. These advantages include lower greenhouse gas emissions, higher power conversion efficiencies, and lower acoustic intensities due to reduced mechanically-generated noise. Notwithstanding challenges facing battery adoption as a primary energy source – lower energy and power densities, limited cyclability, higher safety risks, lower abuse tolerance, and regular maintenance – key players within the aviation industry have committed to pushing for the development of clean technology to meet the ambitious carbon-neutral goals set by IATA [1], NASA [2] and the European Union [3]. Illustrated in Fig. 1, the extensive use of lithium-ion (Li-ion) batteries, in particular, places them at the forefront of many research and development efforts across the electric-aviation ecosystem. However, even with their superiority in performance, safety, reliability, and mass production quality assurance over other battery chemistries, studies indicate that Li-ion batteries designed for aircraft would still need a replacement every three to five months due to an order-of-magnitude increase in heat generated compared to electric vehicles that accelerate energy-storage capacity degradation [4, 5].

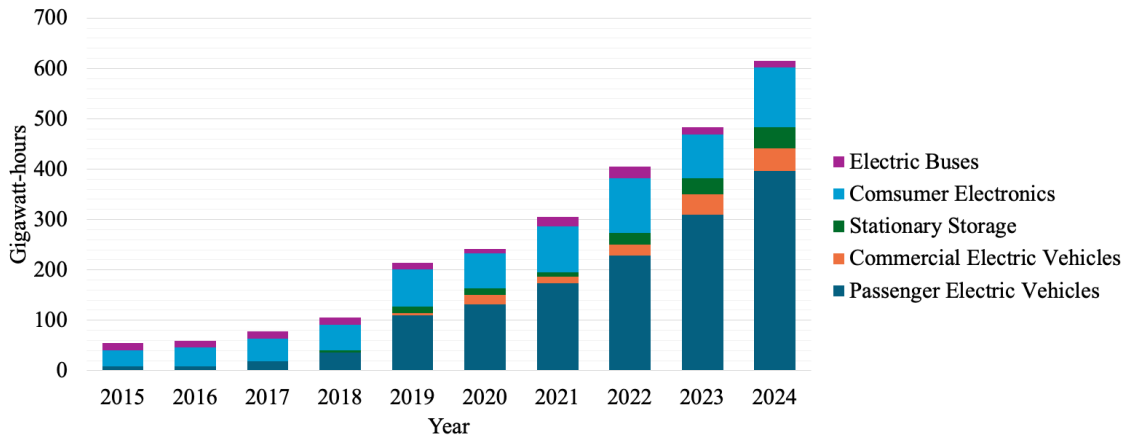


Fig. 1 Annual Lithium-ion battery demand [6].

Compared to hydrocarbon combustion, electrochemical energy conversion is constrained within a thermal range of around 40 degrees. This makes the thermal management of battery cells as crucial as their energy and power density characteristics. The degree to which heat is regulated directly impacts the charging and discharging properties of batteries, their capacity, and their cycle life. This, coupled with the significant variations of operating and ambient conditions, makes the BTMS in an electric aircraft particularly challenging. Unfortunately, conventional aircraft design methodologies, which start with payload requirements and aerodynamics, overlook the strong dependence of the performance of stored energy systems on the temperature and state of health. These factors have all a non-negligible effect on overall aero-propulsive efficiencies, and as such, their negligence can have significant ramifications, as seen from the failures of Airbus' E-Fan X and NASA's X-57 tech demonstrators [7–9].

In surveying the literature, one can point to various sources that explore the thermal management of battery-electric systems, irrespective of the vehicle platform. Many of these various architectures are documented in the review paper by Kim [10] *et al.*, with notable examples provided in [11, 12]. Recent work has also demonstrated the development of a design methodology for clean sheet electrified ground vehicle BTMS designs by introducing a decision tree to enable analysis-driven design space exploration using simulation and modeling tools [13]. Only recently has there been a concerted effort to examine aerospace systems. One of which is [14], who designed a BTMS for a hybrid electric aircraft of similar size to the one in this study. Specific details about the models used to size their BTMS can be found in [15]. Other studies employed semi-empirical models to assess electric aircraft performance over their entire operational lifetime, focusing on cycle discharging, air cooling, and cell aging [16–18]. Bakhshi [19] *et al.* explored various cooling configurations of a graphite-based heat spreader for electric vertical takeoff and landing (EVTOL) aircraft through numerical and experimental means but did not couple their simulations with loads generated by the aircraft during flight. In a later study, Zhao *et al.* [20, 21] built upon the efforts of Clarke [17, 18] to integrate a liquid-based cooling system coupled with a heat exchanger to more effectively cool EVTOL aircraft. Despite successfully predicting changes in required mass flow rates, determining the power required to cool the battery pack, and demonstrating pathways to reduce battery degradation, the thermal regulation computations were also decoupled from flight simulations and the

aircraft's energy-network analyses, implying that the actual state of the battery pack was not computed throughout the flight profile. Leveraging ambient temperature to cool batteries via skin exchangers has also arisen as a pathway to regulate heat from batteries. Previous work by Shekar & Clarke [22] studied the system level impact of a BTMS on an electric aircraft which was based off the NASA X-57 Maxwell, and highlighted the interdependence between the BTMS and the aircraft itself. In a paper by Konig [23] *et al.*, the authors performed a theoretical study to explore the suitability of surface heat exchangers for battery heat rejection. Besides the complicated plumbing system that would be required, implementing such a system using airworthy manufacturing methods of today is highly unlikely at this juncture in time.

This article seeks to build on this relatively adolescent field by extending the work of [14] and [21] by coupling the BTMS operation with the performance of the propulsion architecture within the mission solver that solves the energy network and kinematic equations at each time-step. In doing so, we seek to explore the constraints associated with a fully integrated BTMS and assess the operational ramifications and feasibility of conducting such flights within congested air traffic routes. The taxi and ground segments are included to capture such realism and highlight what decisions a ground operator or pilot may make to ensure that the batteries are sufficiently preheated on a cold day or cooled on a hot day. The remainder of this paper is structured into six sections to answer the following questions:

- 1) How does the operational performance of the BTMS vary with changes in climate, notably ambient temperature?
- 2) With the varying ambient temperature, how does the battery perform, resulting in changes to the flight profile? With these two questions answered it will then lead to a comprehensive understanding of the overarching unknown faced by the aviation industry today, that is:

- 3) When operating out of metropolitan hubs, what regional airports can electric aircraft serve, and how dependent is it on the local climate?

Section II provides the parameterization of the 19-seater regional twin-propeller aircraft used for case studies. This includes high-level aircraft properties and a step-by-step methodology for sizing the individual components of the BTMS. Section III outlines the design considerations to design an electric aircraft and understand how it operates to set a baseline. This is then extrapolated to operate under various operating conditions to identify regions with the most promise for regional air mobility. A comprehensive overview of the results and key findings is provided in Section IV, which will answer the first two questions. Section V answers the third question posed by studying the feasibility of an electric aircraft in replacing conventional aircraft for regional air transportation. This is followed by a plan for future code development and an outline for an experimental campaign to corroborate these computational studies in Section VI.

II. Battery Thermal Management System Design Methodology

A. Aircraft Platform

Before discussing the methodology for sizing a BTMS, we will expand upon the chosen aircraft platform to study sub-component performance. This aircraft was selected from a weight class that has proven to be capable of being electrified using today's technology. Shown in Fig. 2, this was the Viking DHC-6 Series 400 Twin Otter. This high-wing monoplane was retrofitted with an all-electric powertrain, where all the fuel-based propulsion components were swapped with an electric powertrain comprising electric motors, three-bladed Hartzell HC-B3TN-3D propellers, inverters, high voltage cables, batteries, power electronics, and of course, a BTMS. The propellers, each of diameter 2.6 m and a blade angle range of -15° (full reverse) to $+87^\circ$ (feathered), were powered by motors rated at 620 hp. Like the fuel-powered variant, the maximum takeoff gross weight (MTOW) is fixed at 12,500 lbs. Flight simulations were performed using the Research Community Aerospace Interdisciplinary Design Environment (RCAIDE) [24], developed by the Laboratory of Electric Aircraft Design and Sustainability at the University of Illinois, Urbana-Champaign. RCAIDE is the successor to the SUAVE code [25, 26], widely used within the aerospace community for aircraft design, analysis, and optimization. Many of the discipline analyses within RCAIDE have been benchmarked against SUAVE, which itself has gone under significant V&V over the years [27–29].

The BTMS consists of a conjugate cooling wavy channel through which coolant circulates throughout the battery modules of the battery pack. The heated coolant then passes through channels of a fin heat exchanger, before being recirculated back through the wavy channel. The bulk of the coolant is held within polyetherimide reservoirs located in the wings where fuel was once stored, where it is exposed to ambient conditions. A detailed visualization of this cooling cycle is represented in Fig. 3. Here, we see the reservoir as an intermediary step between the cooling and heating stages, allowing for mixing. The BTMS sizing routine aims to fine-tune the geometric properties of the HAS and HEX and the operation of auxiliary devices such as pumps and fans while minimizing overall weight and power

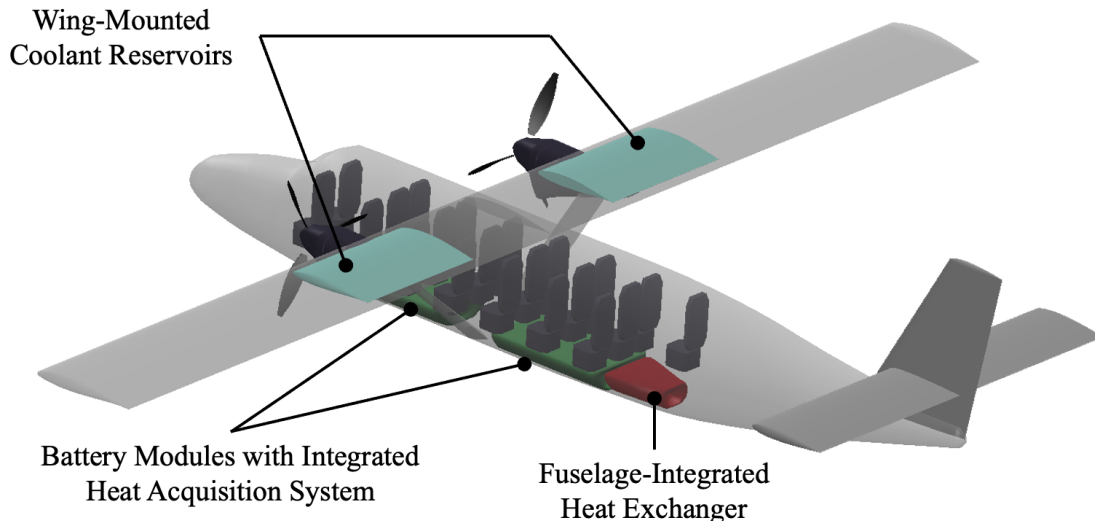


Fig. 2 Electric Twin Otter

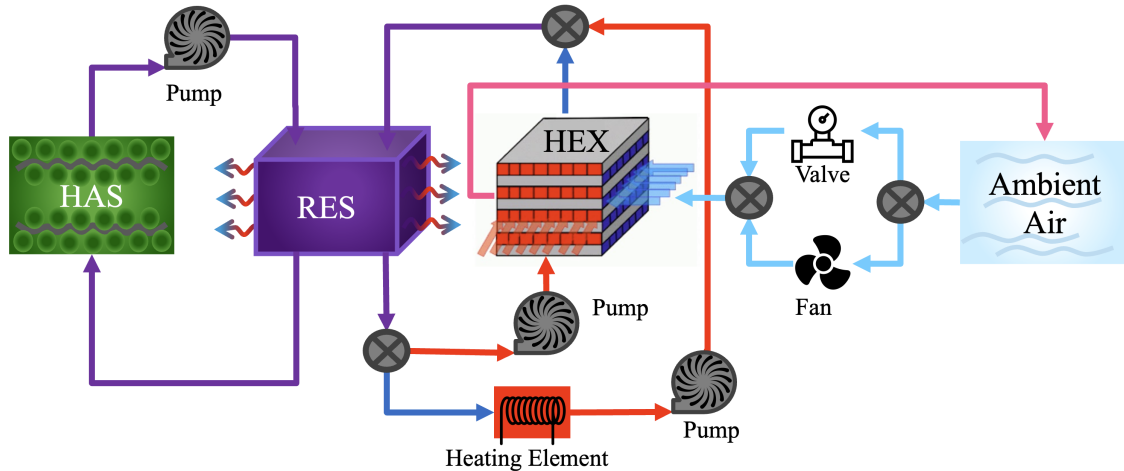


Fig. 3 Battery thermal management system.

consumed. It is bifurcated into two distinct optimization processes, with the outputs from the first being used as inputs for the subsequent optimization process.

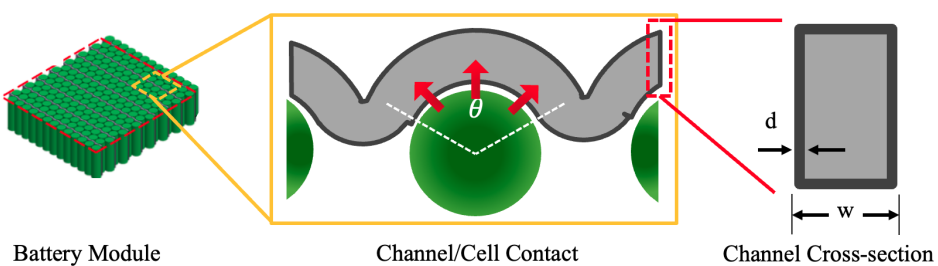


Fig. 4 Wavy channel heat acquisition system.

B. Conjugate Cooling Heat Acquisition System and Auxiliary Pump

Sizing the HAS requires the following properties of the battery pack: thermal load (heat) to be removed, the battery cell type, cell geometry, and the geometric layout of the module in terms of the number of cells in each row and the number of rows. A suitable model for understanding the behavior of this system therefore encompasses a model that can determine the heat produced by cells and a representative model of the small channels that are fitted between the rows of cells. The Lithium Nickel Manganese Cobalt (NMC) battery cell within RCAIDE's battery library was selected for this study. The thermal model for this cell is capable of capturing both joule and entropy heat emanating from the cell. More on this model can be found in [17]. The pack comprised 12 modules connected in series for this aircraft. Each module had 2100 cells connected in $10 s \times 120 p$ electrical arrangement. This was done to ensure that the maximum voltage of each module never exceeds 50 V. More importantly, the cells in each module were arranged in 50 rows, each containing 42 cells.

The design variables for this sizing optimization include the dimensions (θ & d) of the wavy channel as seen in Fig. 4. This plays a vital role in determining the overall battery pack dimensions, as well as the mass flow rate of the coolant. Fig. 5 depicts the pseudocode flowchart of this sizing process. A single constraint requiring the heat generated by the battery (\dot{Q}_{gen}) to be equivalent to the heat (\dot{Q}_{conv}) removed by the wavy channel is instituted. The friction factor and Nusselt numbers used to determine various properties of the system were obtained from Bergman [30]. The authors refer the reader to [17] for expressions of the overall heat transfer coefficient (U_{total}), area of the channel (A_{chan}), and the log mean temperature (T_{lm}). The convected heat from the batteries due to the wavy channel is determined using Eq. (1).

$$\dot{Q}_{conv} = U_{total} \cdot A_{chan} \cdot T_{lm} \quad (1)$$

A weighted exponential sum method is used to accomplish the coupled minimization of the HAS's mass and power consumption. These properties are calculated using Eq. (2) and Eq. (3). Appropriate weighting factors are applied to account for the notable difference in magnitude between mass and power. This approach ensures that the optimizer gives equal importance to both parameters, recognizing their significance in the overall optimization process.

$$M_{HAS} = \rho_{line} \cdot L_{chan} \quad (2)$$

$$P_{HAS} = \frac{\dot{m}_{coolant} \cdot \Delta P_{h, HAS}}{\eta_{tpump} \cdot \rho} \quad (3)$$

During off design operation in flight, the net heat flux within the battery modules is computed as follows:

$$\dot{Q}_{net} = \dot{Q}_{conv} - \dot{Q}_{gen} \quad (4)$$

The changes in the battery's temperature at each discrete time step are determined through the application of Eq. (5). Note that the calculations are done at the module level since the assumption is made that all modules are equivalent. Therefore, the appropriate number of cells ($N = 2100$) should be used. The battery temperature is systematically updated at each time step.

$$\frac{dT_{bat}}{dt} = \frac{\dot{Q}_{net}}{N_{bat} \cdot m_{bat} \cdot c_{pbat}} \quad (5)$$

Again, the battery temperature directly affects the cell's electrical discharge performance, which in turn affects the supplied power to the motors in flight. Coupling thermal management with battery performance is, therefore, the only way to observe interdependent trends.

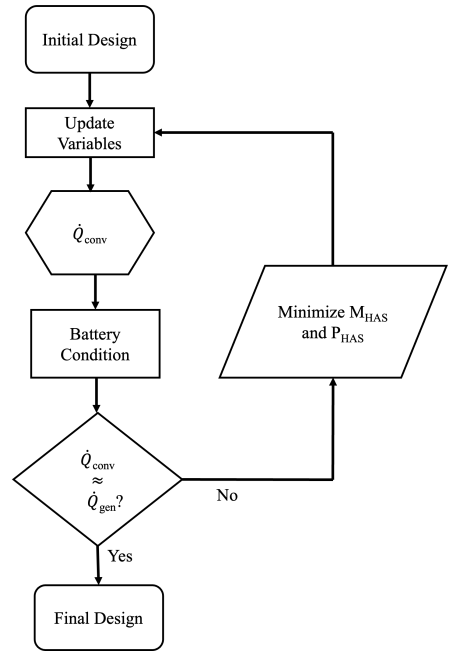


Fig. 5 HAS sizing methodology.

C. Fuselage-Integrated Heat Exchanger System, Auxiliary Puller Fan and Pump

Following a similar approach, the design of the HEX is a dual objective optimization with constraint to maintain the temperature of the coolant less than the temperature of the battery pack. The mass flow rate of the coolant pumped from the reservoir, and the mass flow rate of the air entering through either the ram inlet or the fan and their corresponding inlet pressure are the input variables involved in the optimization of the HEX. The surface designation for a flat plate cross-flow HEX is chosen as a fixed input, drawing upon relevant data such as finned area density and fin thickness [31]. The efficiencies of the pump and the fan used to flow air and coolant through the system, along with the desired efficiency of the HEX, are also defined as fixed inputs in the sizing process. Additional constraints for the sizing problem include the space limitations under the cabin of the fuselage and the upper-performance thresholds of the pump and fan, i.e., their rated pressure ratios.

The determination of the dimensions of the HEX is in itself an iterative process shown in Fig. 6. First, the coolant (h) and air (c) outlet temperatures are determined by Eq. (6) and Eq. (7). The minimum (C_{\min}) and maximum (C_{\max}) heat capacities are subsequently determined to calculate the heat capacity ratio ($C_r = C_{\min}/C_{\max}$).

$$T_{o_h} = T_{i_h} - \varepsilon \cdot (T_{i_h} - T_{i_c}) \quad (6)$$

$$T_{o_c} = T_{i_c} + \left(\frac{\varepsilon \cdot \dot{m}_h}{\dot{m}_c} \right) \cdot (T_{i_h} - T_{i_c}) \quad (7)$$

The number of transfer units is computed using the effectiveness-NTU method, commonly used for analyzing HEX performance for an unmixed cross-flow HEX in Eq. (8) [30]. This step requires finding the unique solution using Python's SciPy's solver [32].

$$\varepsilon = 1 - \exp \left(\frac{(NTU^{0.22})}{C_r} \cdot \left(\exp \left(-C_r \cdot (NTU^{0.78}) \right) - 1 \right) \right) \quad (8)$$

To compute the initial core mass velocity using Eq. (9), the following initial conditions of $j_{f_{h,c}} = 0.25$, $ntu_h = 2NTU$, and $ntu_c = 2C_r NTU$ were chosen. The initial fin efficiencies are also assumed to be 0.8, as indicated in [31].

$$G_{h,c} = \sqrt{2\rho_{m_{h,c}} \frac{\Delta P_{h,c}}{(Pr_{h,c})^{2/3}} \frac{\eta_{o_{h,c}} \cdot j_{f_{h,c}}}{ntu_{h,c}}} \quad (9)$$

The Colburn and friction factors are updated using empirical relations obtained from [31]. These require first solving for the Reynolds number. The fin efficiency is then re-evaluated in Eq. (11) for both the hot and cold sides of the HEX, which is based on the heat transfer coefficients derived in Eq. (10), providing a more accurate estimate of the fin efficiency, which is computed in Eq. (11) under updated thermal conditions.

$$h_{h,c} = j_{h,c} \cdot G_{h,c} \cdot c_{p_{h,c}} \cdot (Pr_{h,c})^{2/3} \quad (10)$$

$$(\eta_f)_{h,c} = \frac{\tanh((m_f)_{h,c} \cdot (l_f)_{h,c})}{(m_f)_{h,c} \cdot (l_f)_{h,c}} \quad (11)$$

With this, the lengths of the coolant and air sections and the height of the HEX depicted in Fig. 7 can be computed using Eq. (12).

$$L_{h,c} = \frac{d_{h,c} \cdot A_{h,c}}{4A_{o_{h,c}}}, H_{h,c} = \frac{A_{f_{c,h}}}{L_{h,c}} \quad (12)$$

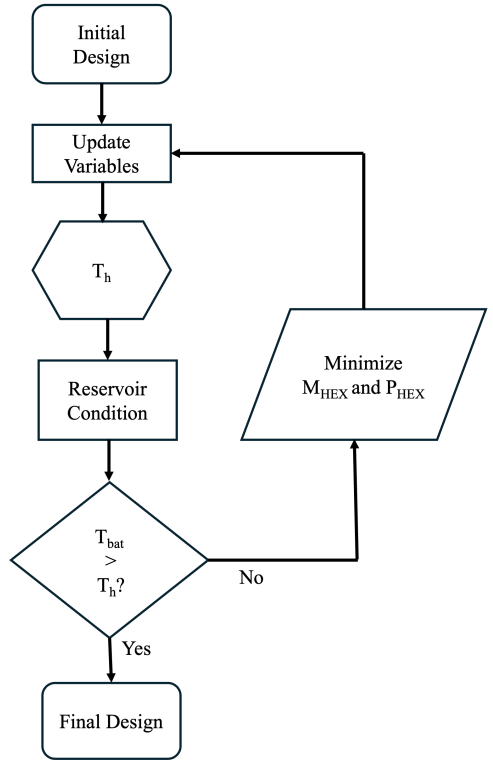


Fig. 6 HEX sizing methodology.

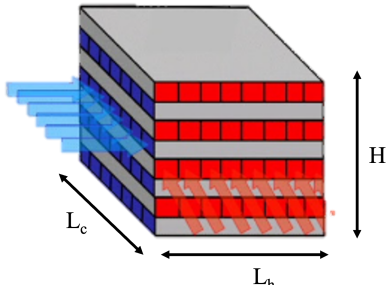


Fig. 7 HEX dimensions.

, where

$$A_{h,c} = \frac{NTU \times C_{h,c}}{U_{h,c}}, A_{o_{h,c}} = \frac{\dot{m}_{h,c}}{G_{h,c}} \quad (13)$$

The resulting pressure differences on the coolant and air sections are evaluated from Eq. (14). The friction factor is empirically corrected to account for the effect of wall temperature. The entrance and exit coefficients are evaluated to be as follows:

$$\begin{aligned} \Delta P_{\text{new}(c,h)} &= \frac{G_{c,h}^2}{2\rho_{c,h_i}} \left((1 - \sigma_{c,h}^2 + k_{c,c,h}) + 2 \left(\frac{\rho_{c,h_i}}{\rho_{c,h_o}} - 1 \right) \right) \\ &\quad + f_{c,h_{\text{wall}}} \cdot 4 \frac{L_{c,h}}{d_{h,c}} \frac{\rho_{c,h_i}}{\rho_{c,h_m}} - (1 - \sigma_{c,h}^2 - k_{e_{c,h}}) \frac{\rho_{c,h_i}}{\rho_{c,h_o}} \end{aligned} \quad (14)$$

, where $K_{c_{h,c}} = 0.36$ and $K_{e_{h,c}} = 0.42$ from [31].

These computed pressure differences, obtained from Eq. (14), are checked against the rated pressure ratios of the components. The sizing process repeats by calculating core mass velocities using Eq. (9) with the new pressure differential. This loop continues until the pressure difference is within 0.01 Pa of the specified value. Once a satisfactory convergence is achieved, the dimensions obtained are cross-referenced to the constraints defined. With the dimensions of the HEX determined, the power and mass of the HEX are found using Eq. (15) and Eq. (16). The mass and power obtained are fed into the optimizer to minimize both power and mass. Again, appropriate weight factors are applied within the weighted sum optimization algorithm to address the significant difference in magnitude between mass and power in the HEX. This ensures equal consideration by the optimizer, acknowledging the importance of both parameters in the optimization process.

$$M_{\text{HEX}} = \rho_{\text{HEX}} \cdot V_{\text{HEX}} \cdot (1 - \sigma_c - \sigma_h) \quad (15)$$

$$P_{\text{HEX}} = \frac{\dot{m}_h \Delta P_h}{\eta_{\text{pump}} \rho_{h_m}} + \frac{\dot{m}_c \Delta P_c}{\rho_{c_m}} + \frac{u_i^2 - u_o^2}{2\eta_{\text{fan}}} \quad (16)$$

To obtain the performance characteristics of the HEX during off-design conditions (i.e., flight), an initial conservative estimate of 0.75 for the HEX's effectiveness is first assumed. This is iteratively solved to obtain the actual effectiveness of the HEX using Eq. (8). The pressure differential across the cold and hot sides are subsequently computed iteratively using Eq. (14). This process culminates with obtaining the power consumed by the HEX at each control point for a given flight profile.

D. Coolant Reservoir

A thermal management system that leverages existing fuel tanks as reservoirs for coolant storage is proposed as an innovative strategy for accelerating early adoption since no significant component installations would be required. Moreover, coupling the bulk fluid storage loads with the lift-generating structures (wings) can promote wing-root bending moment relief similar to fuel tanks in conventional aircraft. To provide insulation and reduce the risk of freezing at cold temperatures or vaporization in extreme heat in the ground, the reservoir is constructed out of Polyetherimide, with a thermal conductivity of $2.0\text{W}/\text{m} - \text{K}$. Therefore, the external temperature at altitude affects the reservoir's temperature via conduction through the aluminum wing skin. This allows for passive cooling of the coolant, which aids in reducing the size of the heat exchanger, consequently lowering the aerodynamic cooling drag penalties. Outside of the efficiency factors for the pump and fan, the flight simulations did not consider the coolant's friction losses or the weight of the plumbing system required for supplying the coolant to and from the various subsystems around the airframe.

III. Flight Profile Analysis

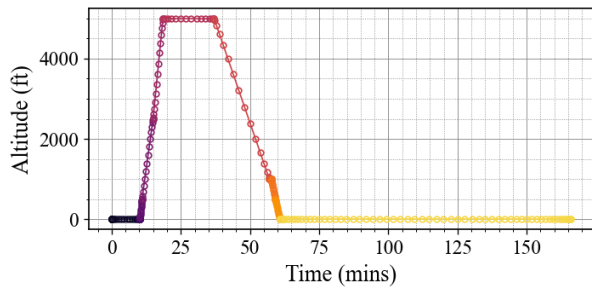
The simulated flight comprised 14 flight segments, 6 of which are ground-based. The kinematics of each segment are listed in Table 1 below, where each row is color-coded to aid in identifying segments in subsequent figures within this paper. Moreover, the ground-based segments are shaded gray for additional distinction. As will be discussed in the results, including ground segments is critical for assessing the practical limits of operation of electric aircraft, particularly in larger airports where ground traffic can be greater than 30 minutes [33]. Of the segments, the cruise leg is modified to meet the range while the idle segment is varied to either limit overheating or permit warming up of batteries before takeoff. The remaining segments were held fixed. However, as will be discovered in Section IV, this

constraint was relaxed in cruise. As such, it is listed in the table with [*]. Recharging at the end of each flight occurred at 1C, or 456A, implying a charging time of 1.75 hrs. Recharging is halted once the batteries hit 100% SOC to avoid overcharging, while the BTMS continues to cool the battery pack for the remainder of the time allotted for recharging.

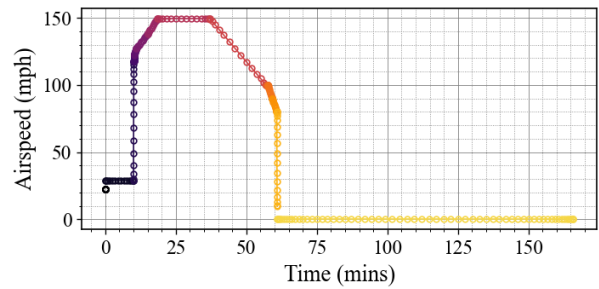
This study does not model the emergency reserve leg that captures either an airport diversion or loiter. It was assumed that the aircraft possessed a small turboelectric generator capable of supplying emergency power to the motors

Table 1 Regional commuting flight profile.

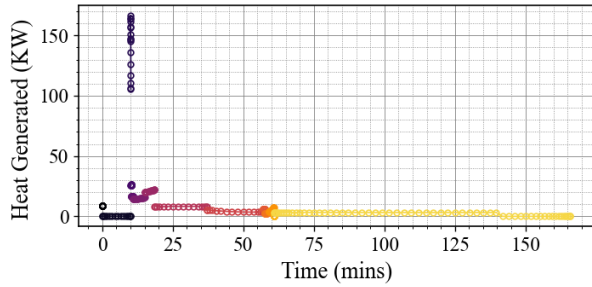
Segment No.	Segment Type	Initial Altitude (ft)	Final Altitude (ft)	Initial Speed (mph)	Final Speed (mph)	Climb Rate (ft/min)
1	Idle	0	0	0	0	0
2	Taxi	0	0	30	30	0
3	Takeoff (Ground Roll)	0	0	30	118	0
4	Departure End of Runway	0	50	118	122	700
5	Initial Climb Area	50	500	122	127	600
6	Low Altitude Climb	500	2500	127	138	500
7	High Altitude Climb	2500	5000	138	150	500
8	Cruise	5000	5000*	150	150	0
9	Descent	5000*	1000	150	115	-200
10	Downleg	1000	1000	115	115	0
11	Baseleg	1000	500	115	90	-350
12	Final Approach	500	0	90	80	300
13	Landing	0	0	0	0	0
14	Recharge	0	0	0	0	0



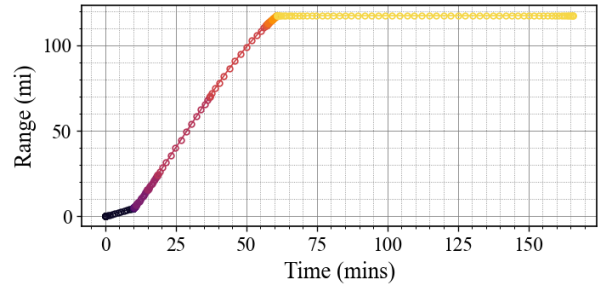
(a) Altitude.



(b) Airspeed.



(c) Battery pack generated heat.



(d) Cumulative range.

Fig. 8 Nominal flight profile of the electric 19-seater commuter aircraft.

in the event of a route diversion. Fuel for such a scenario can be held within the wings as well. Moreover, it should be noted that the electric aircraft in question is designed to be thermally "self-reliant," meaning that even during ground segments like recharging, no additional cooling equipment needs to be provided. This design choice was made considering that the aircraft will be operating in small regional airports that might not have the capabilities for external thermal management systems.

A preliminary mission was simulated to quantify the heat generated by the battery pack throughout the flight to determine the exact design point of the BTMS for the electric Twin Otter. Figs. 8a and 8b depicts the altitude and airspeeds, respectively. Illustrated in Fig. 8c, the generated heat exceeded 100kW during the completion of the departure end of runway segment. However, this represents only a small fragment of the entire mission, and designing a BTMS to extract such a substantial amount of heat would be illogical. The heat generated at the top of the climb is 20kW, which was also initially considered as a reference point for sizing the BTMS. Ultimately, the design point of 25kW was chosen for the BTMS. The design process follows the methodology previously discussed. As stated before, though it is designed to extract 25kW, leveraging the ambient conditions at higher altitudes allows the BTMS to run at a fraction of its designed conditions for most flight segments, particularly long durations such as cruise and descent. As shown in Fig. 8d, the range of the aircraft reaches 110 miles, highlighting the BTMS's efficiency in managing thermal load without excessive battery drain. With the BTMS not consuming its design power throughout, the range of the aircraft can be maximized. The battery packs' end-of-mission SOC is approximately 15%, depicted in Fig. 9a. Throughout the flight, each cell reaches a maximum temperature of 26°C at the top of the climb and is brought back to ambient conditions after charging. This is depicted in Fig. 9d.

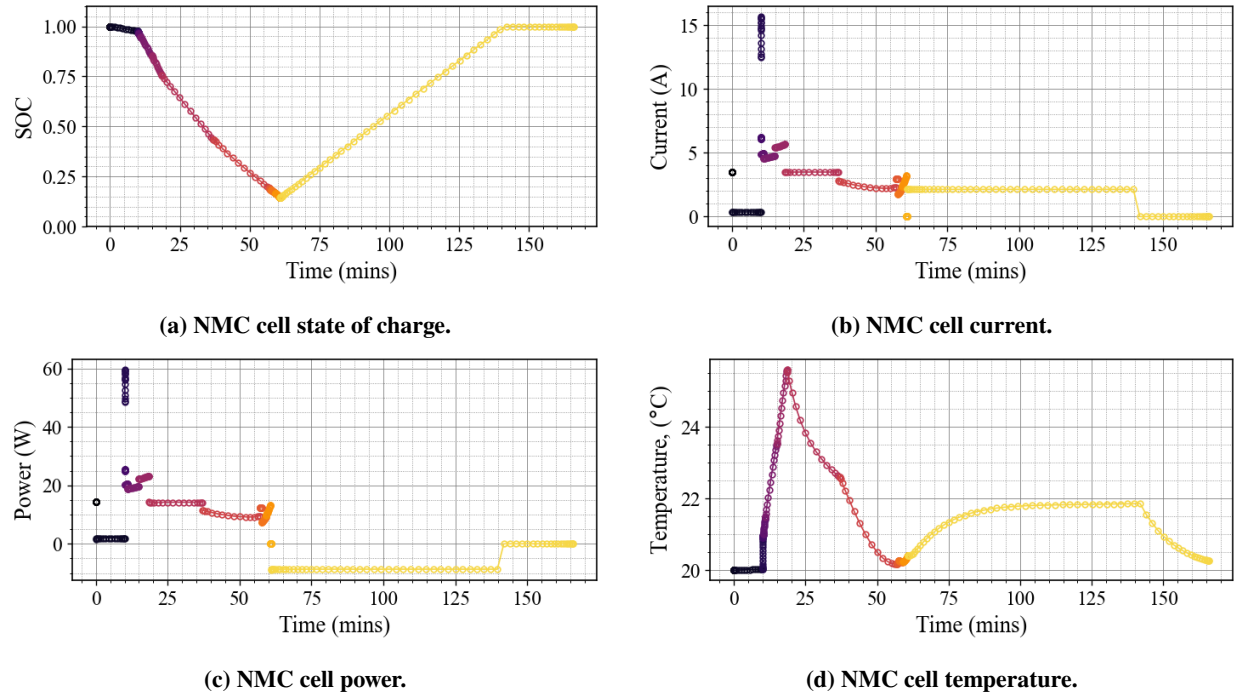


Fig. 9 Baseline cell characteristics.

Regional Operations

With a baseline established, the electric Twin Otter is simulated under various flight scenarios to evaluate its operational flight envelope. The aircraft is tested for takeoff from major metropolitan hubs, including the New York Metropolitan Area (JFK), the Chicago O'hare region (ORD), the San Francisco Bay Area (SFO), the Greater Los Angeles Area (LAX) and the Dallas/Forth Worth Metroplex (DFW). In addition to these cities, a feasibility study is conducted to determine whether this electric aircraft is suitable for regional operations in the Eastern Midwest region comprising cities like Memphis, Louisville, Nashville, St. Louis, Cincinnati, Columbus, and Champaign-Urbana. A key factor under examination in this study is the impact of ambient temperature on the BTMS and overall aircraft

performance. The variation in mean temperature across the 2023 calendar year was used, depicted in Fig. 10. For this study, a temperature range from -5°C to 30°C is considered. The BTMS needs to be optimized to maintain the battery pack within its ideal operating window of 20°C to 30°C while ensuring the aircraft concludes the mission with a state of charge (SOC) of 15%. The impact of ambient temperature on the range is extensively studied, analyzing how the BTMS performs under varying conditions to keep the battery pack within the desired temperature range.

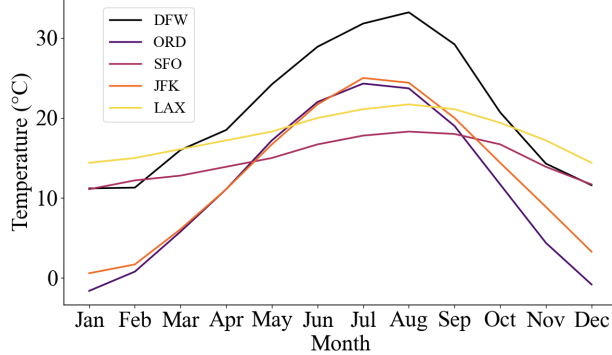


Fig. 10 Variation in ambient temperature across multiple cities in 2023.

IV. Discussion of Results

Operating parameters for the electric Twin Otter were established to simulate real-world conditions at major transit hubs. The operational window was defined as 0600 to 2200 hours, accommodating six flights within a 16-hour period. This schedule accounts for necessary turnaround times between flights, including charging and maintenance procedures. The first flight of each day is denoted the "origination flight," during which the battery pack's temperature is assumed to be equivalent to the ambient temperature. For electric aviation purposes, temperature thresholds have been redefined to account for the unique thermal dependencies of the battery pack. An origination flight is considered a "cold-day" start if the ambient temperature is less than 10°C , while it is classified as a "hot-day" start if the temperature exceeds 28°C . These temperature ranges differ from conventional aviation standards to reflect the heightened thermal management requirements of an electric aircraft battery system. This scenario presents a challenge for the BTMS, as it must efficiently bring the battery pack within its optimal operating temperature range during its origination flight. Subsequent flights benefit from the thermal conditioning achieved during the origination flight, with the battery pack maintained within its ideal temperature window. As inferred in Section III, the BTMS is designed to extract 25 kW of heat. However, continuous operation at this design power is not necessary throughout the flight. By leveraging the reservoir's exposure to the environment, the battery pack can be cooled more efficiently.

A. Component Analysis

Reservoir Analysis

The reservoir plays a critical role in the BTMS's efficiency and adaptability. Its exposure to the environment creates a dynamic thermal coupling that significantly influences the system's performance across various operating conditions. During hot-day starts, as the aircraft gains altitude, the reservoir naturally cools due to decreasing atmospheric temperatures. This phenomenon reduces the load on the BTMS, allowing for more efficient operation. Conversely, in cold-day starts, the BTMS must be operated judiciously to prevent "overcooling" of the battery pack, which could negatively impact performance. Fig. 11 illustrates the variation in coolant temperature within the reservoir as it responds to changes in ambient temperature throughout the flight profile. Fig. 11a specifically demonstrates the effects of an origination flight with a cold-day start, where low ambient temperatures result in cooler coolant temperatures during high-altitude operations. This trend extends to subsequent flights over the 16-hour operational window, with slightly elevated coolant temperatures during cold-day operations as a result of how the BTMS is operated, as seen in Fig. 11b.

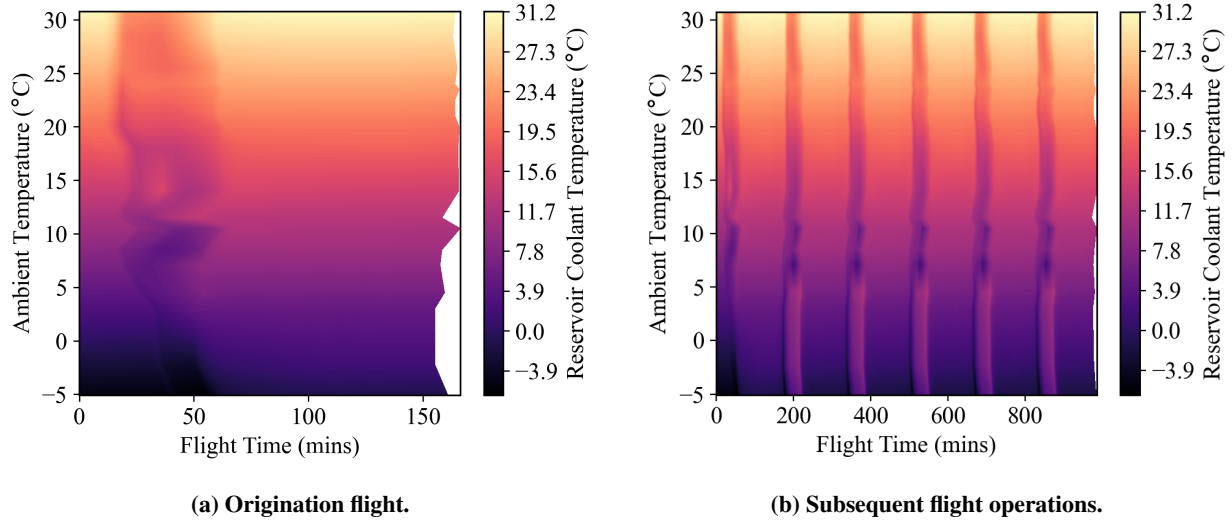


Fig. 11 Reservoir operating conditions.

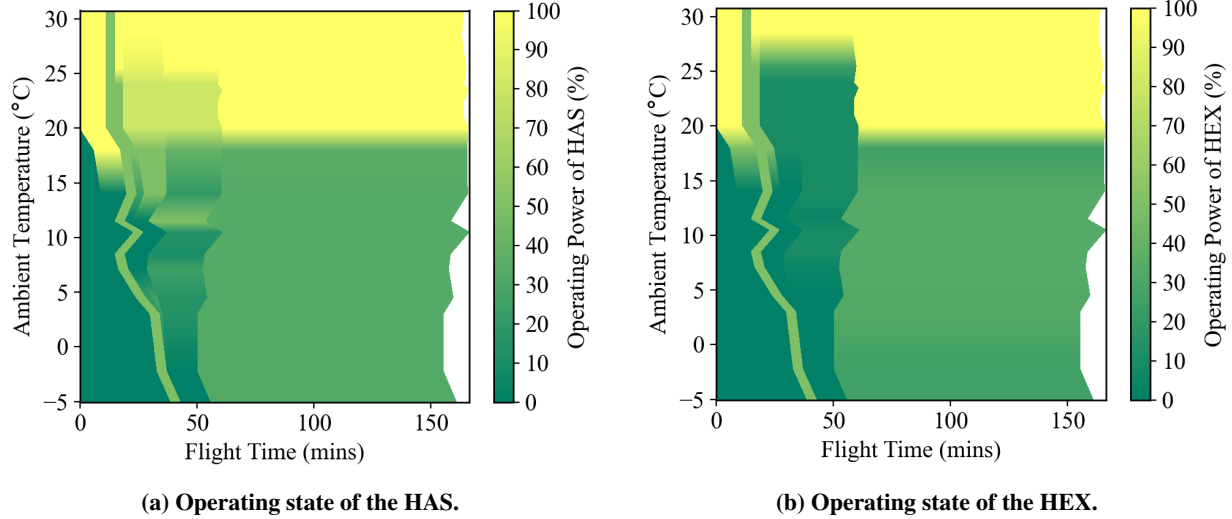


Fig. 12 Origination flight BTMS operating conditions.

Heat Acquisition and Heat Exchanger Analysis

The operation of the HAS and HEX vary significantly based on ambient temperatures and flight phases seen in Fig. 12. This variation is crucial for maintaining optimal battery pack temperatures across diverse operational conditions. During cold-day starts, when the battery pack temperature is below its ideal operating range, significant idle time on the ground is necessary to reach a flight-ready battery temperature of 20°C. During this warm-up period, neither the HAS nor the HEX are operated, as illustrated in Fig. 12a and Fig. 12b. Conversely, on days with high ambient temperatures, both the HEX and HAS operate at full design power throughout the flight to extract sufficient heat and maintain the lowest possible battery temperature. The HAS and HEX operate under different conditions during flight, primarily due to variations in the coolant temperature within the reservoir and the operation of the ram air inlet during high-altitude flight. This operational difference is most pronounced for flights operating in the ambient temperature range of -5°C to 25°C. As ambient temperatures rise above 25°C, both the HAS and HEX need to operate at their full design power to maintain the battery pack within its operational temperature window.

The power consumed by the HAS and HEX varies depending on ambient temperature and flight phase. Fig. 13 illustrates how these two systems' operating conditions change with ambient temperature variations throughout the day.

Notably, during colder day operations, both systems operate at less than half of their designed power. In low-temperature scenarios, precise modulation of the BTMS is critical. The heat removal rate must be carefully controlled to prevent the battery temperature from dropping below acceptable limits, ensuring optimal performance without risking degradation due to overcooling. Conversely, when operating in higher ambient temperature ranges, the HAS and HEX need to be operated at their design power for the majority of the day to maintain proper thermal management.

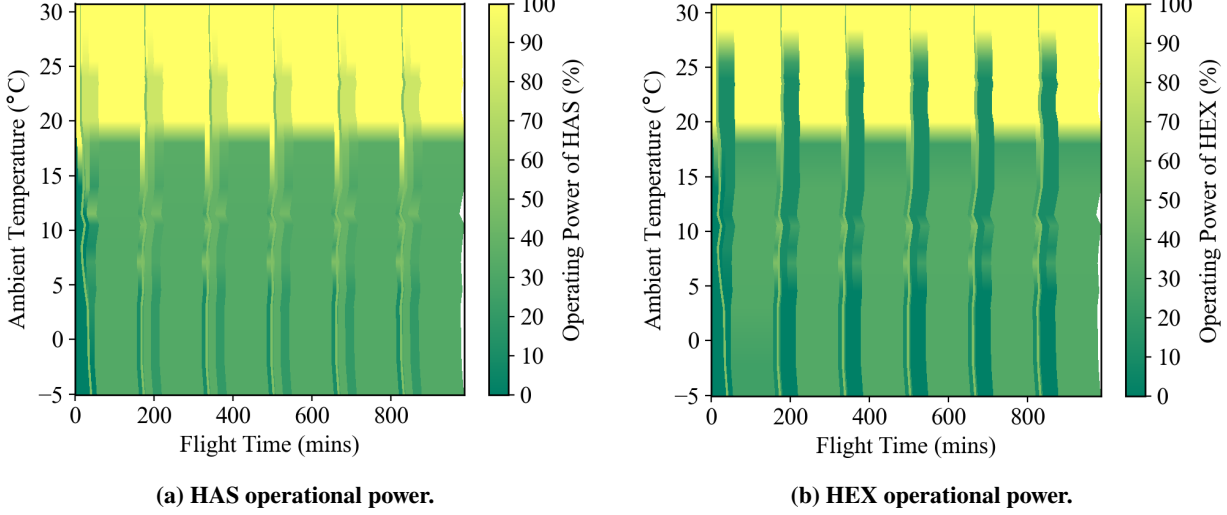


Fig. 13 Subsequent flight BTMS operating conditions.

Battery Performance Analysis

The previous sections described how the BTMS operates based on the reservoir temperature and the ambient temperature. Fig. 14 illustrates the variation in battery temperature under different scenarios. During cold-day starts, the battery temperature is intentionally raised to about 20°C during the idling phase. During the long idling phase (low ambient temperatures), the range of the aircraft is reduced as a result, and in some cases, the ceiling altitude of the aircraft had to be reduced to as low as 2750 ft in order to complete the flight a 15% SOC. As the ambient temperature increases, the duration of this idling phase decreases, as demarcated by the white line in Fig. 14a. However, during

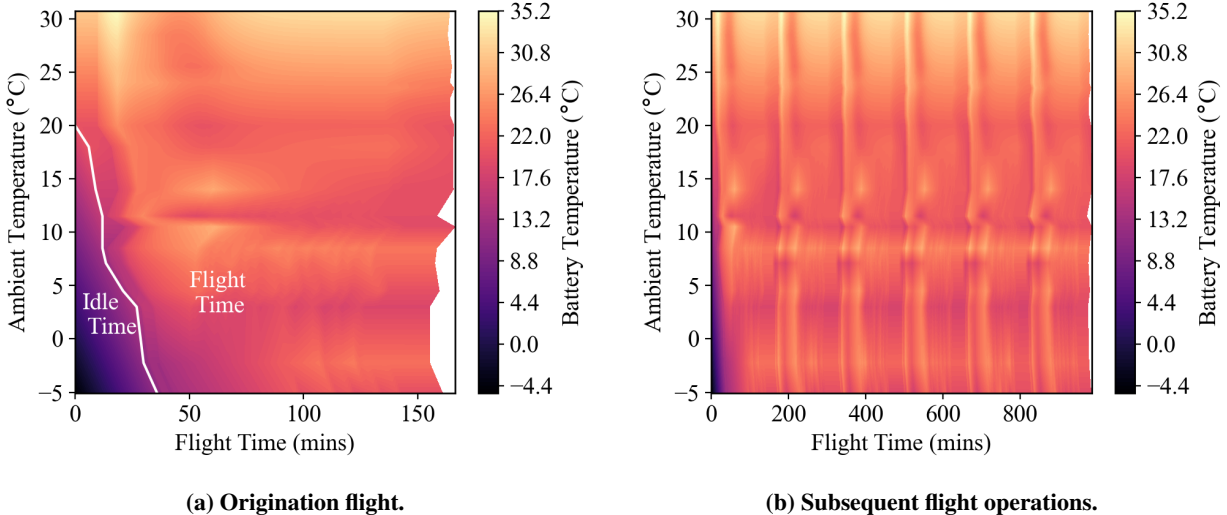


Fig. 14 Battery operating conditions.

hot-day starts, it is noted that at the top of climb, the battery temperature can exceed 35°C. This issue cannot be fully mitigated in the current BTMS design due to limitations imposed by the ambient temperature in which the aircraft operates. The white regions in Fig. 14a represent periods when the flight is terminated early due to earlier depletion of the battery pack. Figure 14b demonstrates the variation in battery temperature after the origination flight. Flights following cold-day starts are able to regulate the battery temperature within its ideal operating window due to the optimized operation of the BTMS. However, after a hot-day start, the battery temperature for subsequent flights cannot always be maintained within the ideal operational window. This is primarily due to the long recharge segment on the ground. Although the batteries are precooled right before landing by leveraging the cold air available at higher altitudes, the heat generated during charging negates this effect. Consequently, after charging, the batteries approximately return to a temperature equal to the ambient temperature, with constant cooling. This is in line with the design philosophy of not employing external cooling mechanisms and relying on the aircraft BTMS, which limits the cooling to the ambient temperature.

V. Implications on Flight Operations

Through Section IV, an in-depth overview was provided on how the BTMS acts under various conditions. This section will examine the system-level impact of these operations. These system-level impacts refer to the highly coupled nature of the components. The power consumed by the BTMS is drawn from the batteries themselves, which in turn produces additional heat. Furthermore, when the HEX operates in its ram inlet mode, the resulting drag is accounted for in the mission solver, leading to increased thrust requirements. This increased thrust is produced by drawing more current from the battery, which again leads to an increase in heat generated by the battery pack. The temperature profile of the battery across the flight segment impacts battery performance. Fig. 15a captures the range achieved when flights are operated across different ambient temperatures while also showing the variation in battery temperature. In the case of a cold-day start with an initial temperature of -5°C , the idle segment depletes the battery pack significantly, resulting in a range of only 35.5 miles. This low range is primarily due to the idling segment but also because the batteries are required to operate at the lower end of their operational temperature spectrum, leading to decreased efficiency over the origination flight. The range of the aircraft increases with rising ambient temperature, achieving a maximum of 112 miles for the origination flight when the ambient temperature is 20°C . As the ambient temperature rises further during hot-days, a dip in the range is observed. When the ambient temperature reaches 30°C , the range drops by 10 miles. This decrease is due to two reasons: firstly, the increased power demands of the BTMS itself, which draws excessive power from the batteries to keep the battery pack cool, and secondly, the operating temperature range of the battery. It is observed that during the top of climb, the battery temperature reaches a maximum of 35°C, leading to decreased battery efficiency that impacts the overall range for the origination flight.

For subsequent flights, as shown in Fig. 15b, hot-day flights see a decreased range compared to other flights. This is

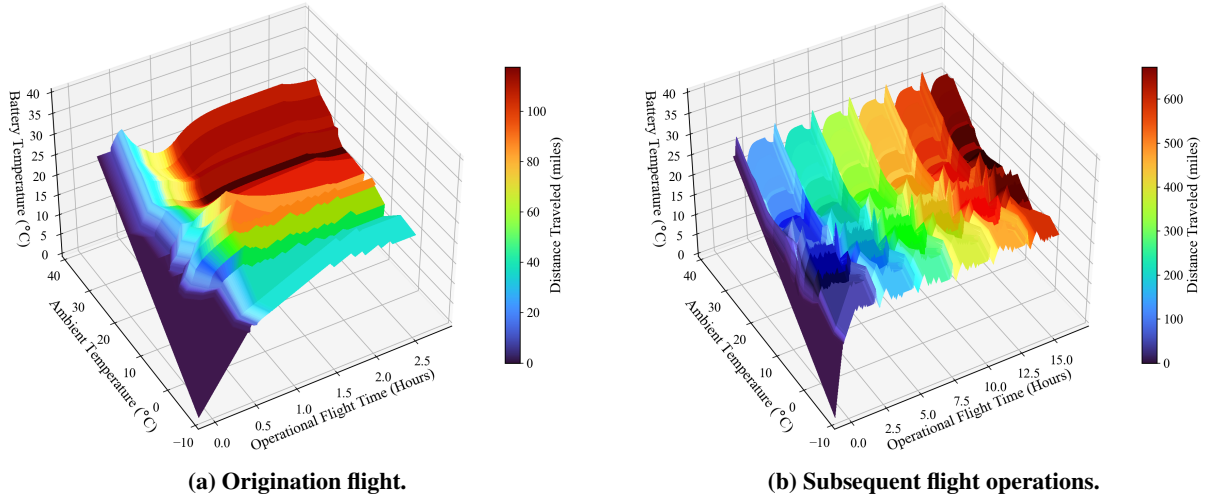


Fig. 15 Impact of ambient and battery temperature on the overall range.

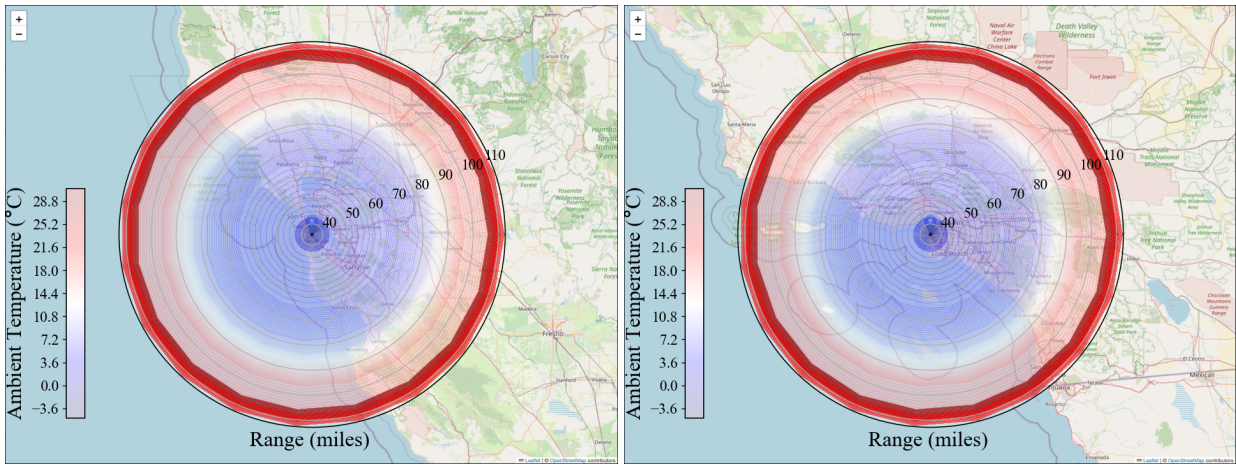
due to the high temperatures reached by the battery pack during the top of climb, which leads to decreased efficiency of the batteries. For all subsequent flight operations, the batteries start their mission at a temperature of 20°C or the ambient temperature, whichever is higher. This temperature management results in optimal performance for all flights following the origination flight, except those conducted in hot-day conditions.

The fundamental questions listed in Section I are addressed based on this comprehensive analysis conducted. The first question is answered through the examination of BTMS operational parameters across various flight segments in Section IV, revealing the system's dynamic performance under different conditions. This leads to the second question, addressed in this section, which provides insights into how operational parameters affect flight profiles for both origination and subsequent flights, demonstrating the BTMS's influence on the aircraft's range and mission capabilities under varying environmental conditions.

Impact on Regional Flight Operations

To study the impact of electric aircraft on regional operations out of the major hubs listed in Section III, it's important to note that the change in range primarily affects the origination flight, as subsequent flights maintain a similar range once the battery pack reaches its optimal temperature. This examination highlights the relationship between local climate conditions and the electric aircraft's operational capabilities, providing a clear picture of the potential range and serviceable regional airports from each hub, as illustrated in Fig. 16. The overlay of the range of the aircraft is performed on maps obtained from Follium [34]. Fig. 16a overlays the aircraft's range variation with ambient temperature on a map of the San Francisco Bay area, originating from San Francisco International Airport (SFO). During cold-day starts, Oakland International (OAK) and San Jose International Airports (SJC) are within range. As temperatures rise, increasing the range to 80 miles, Charles M. Schulz–Sonoma County Airport (STS) in Santa Rosa and Monterey Regional Airport (MRY) become accessible. At ideal temperatures, when the electric aircraft achieves maximum range, airports like Sacramento International (SMF) come into play. Similarly, for flights from Los Angeles International Airport (LAX) in Fig. 16b, cold-day starts allow flights to Burbank Bob Hope Airport (BUR), Long Beach Airport (LGB), and John Wayne Airport (SNA). At the 80-mile mark, Santa Barbara Airport (SBA) and Meadows Field in Bakersfield (BFL) become reachable. When the range extends to 100–110 miles, San Diego International Airport (SAN) enters the operational sphere.

Fig. 16c illustrates the operational range from John F. Kennedy International Airport (JFK) based on ambient temperatures. During cold starts, nearby airports such as LaGuardia (LGA) and Newark Liberty (EWR) are accessible. Long Island MacArthur (ISP) and Philadelphia International (PHL) become reachable as temperatures rise and the range increases. At maximum range in warmer conditions, airports like Bradley International (BDL) and Albany International (ALB) are within range. Fig. 16d demonstrates the operational range from Dallas/Fort Worth International Airport (DFW) as influenced by ambient temperatures. In colder conditions, the range includes nearby airports such as Dallas Love Field (DAL) and Fort Worth Meacham (FTW). As temperatures increase, extending the range, airports like Waco Regional (ACT) and Tyler Pounds Regional (TYR) become accessible. At the highest range in warmer conditions, the range expands to include airports such as Abilene Regional (ABI) and Longview East Texas Regional (GGG).



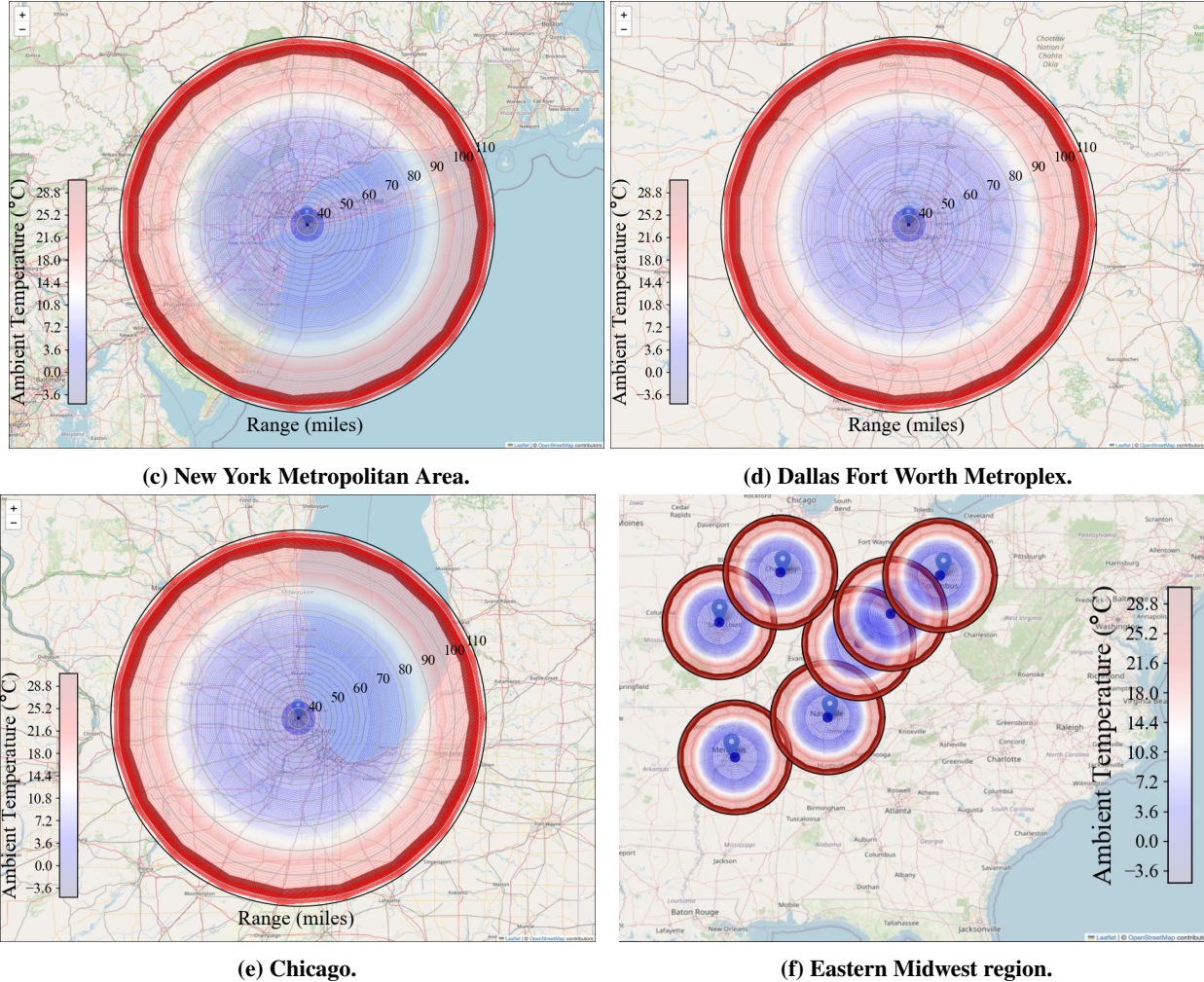


Fig. 16 Aircraft flight range given ambient temperature.

While flying out of Chicago O'Hare International Airport (ORD) as shown in Fig. 16e, frigid conditions increase the likelihood of limited travel. Flights to South Bend International Airport (SBN) and Milwaukee Mitchell International Airport (MKE) are feasible when conditions are favorable. However, flights to destinations such as Bloomington IL, Champaign-Urbana IL, Peoria IL, Lafayette IN, and Fort Wayne IN are not possible. A closer look at whether this electric aircraft can serve the eastern Midwest region, as depicted in Fig. 16f, reveals that the results are not promising due to the significant distances between major cities. For routes originating from cities such as Memphis (MEM), Louisville (SDF), Nashville (BNA), St. Louis (STL), Cincinnati (CVG), Columbus (CMH), and Champaign (CMI), it is evident that even under ideal weather conditions, most of these routes are not feasible. Flights operating between Cincinnati, Columbus, and Louisville are the only viable routes.

VI. Future Work

Varying operational conditions present unique challenges in designing electric aircraft compared to conventional ones. With the growing emphasis on alternative energy pathways to replace conventional hydrocarbon derived aviation fuels, electric aviation emerges as a serious contender. In this study, we perform a systems-level analysis of the impact that the battery and the BTMS, coupled with operating conditions, have on the operational viability of routes. Further work needs to be done to increase the range of such aircraft, so that it can cater to a wider segment of the population, not only in the United States but also wherever regional air travel can be electrified. Additionally, advances in thermal management technologies, such as integrating phase change materials for heat transfer or micro-cooling systems, could

be game changers. To sum it up, we also need to assess how long an electric aircraft equipped with batteries can operate under varying conditions. Accurately determining the life of an electric aircraft's battery pack before it needs replacement is crucial for performing an accurate cost analysis. This holistic approach will play an important role in making electric aviation accessible to people of all classes throughout the world.

VII. Conclusion

The fundamental questions motivating this research can now be answered based on the comprehensive analysis conducted. The first question posed was how the operational performance of the battery thermal management design varies with changing operating conditions. This question is answered by thoroughly examining the BTMS operational parameters across various flight segments in Section IV. The analysis reveals the dynamic nature of the BTMS performance as it adapts to different ambient temperatures and flight phases. This comprehensive analysis naturally leads to addressing the second question, which was, considering climate, how does the battery performance result in changes to the flight profile? This is answered in Section V, which provides insights into the variation of operational parameters and their impact on the flight profile, not only for the origination flight but also for subsequent flights. A look at the feasibility of regional operation across various states suggests that the impact of the electric twin-otter serving densely populated areas with multiple cities in the vicinity can be pretty significant. Even during cold day starts, when an aircraft departs from cities like San Francisco or Los Angeles, it can serve nearby destinations effectively. These cities have a compact layout and a higher number of proximate destinations within the aircraft's range, making them ideal for the Twin Otter's operational efficiency. However, in the case of Chicago, the area it covers is too large. The expansive geography and dispersed layout of potential destinations present challenges, particularly during cold day starts. This means fewer nearby destinations can be serviced efficiently, limiting the operational impact of the electric twin-otter in such scenarios, which concludes by sufficiently answering the third question posed.

VIII. Acknowledgements

The authors would like to thank the NSF-funded ERC, the Center for Power Optimization of Electro-Thermal Systems, Project R1.023.23, for their financial support during the research. The authors also acknowledge the contributions of Dr. Nenad Miljkovic and Dr. Chunrong Zhao for their invaluable insights.

References

- [1] International Air Transport Association, “Net zero carbon 2050 resolution,” , April 28 2024. URL [https://www.iata.org/en/iata-repository/pressroom/fact-sheets/fact-sheet---iata-netzero-resolution/](https://www.iata.org/en/iata-repository/pressroom/fact-sheets/fact-sheet---iata-net-zero-resolution/), [Online].
- [2] European Commission, Directorate-General for Mobility and Transport, Directorate-General for Research and Innovation, “Flightpath 2050 : Europe’s vision for aviation : maintaining global leadership and serving society’s needs,” , April 28 2024. URL <https://www.nasa.gov/wp-content/uploads/2023/04/advancing-nasas-climate-strategy-2023.pdf>, [Online].
- [3] European Commission, Directorate-General for Mobility and Transport, Directorate-General for Research and Innovation, “Flightpath 2050 : Europe’s vision for aviation : maintaining global leadership and serving society’s needs,” 2011.
- [4] Gray, J. S., Hwang, J. T., Martins, J. R. R. A., Moore, K. T., and Naylor, B. A., “OpenMDAO: an open-source framework for multidisciplinary design, analysis, and optimization,” *Structural and Multidisciplinary Optimization*, Vol. 59, 2019, pp. 1075–1104. <https://doi.org/10.1007/s00158-019-02211-z>.
- [5] Yang, X.-G., Liu, T., Ge, S., Rountree, E., and Wang, C.-Y., “Challenges and key requirements of batteries for electric vertical takeoff and landing aircraft,” *Joule*, Vol. 5, 2021, pp. 1644–1659. <https://doi.org/10.1016/j.joule.2021.05.001>.
- [6] Wang, B., “World Battery Production,” , Feb 2020. URL <https://www.nextbigfuture.com/2020/02/world-battery-production.html>.
- [7] Airbus, “E-Fan X Hybrid-Electric Propulsion Aircraft,” , 2023. URL <https://www.aerospace-technology.com/projects/e-fan-x-hybrid-electric-aircraft/>, [Online].
- [8] Kuhr, J., “NASA Axes its X-57 Maxwell Electric Aircraft,” , June 26 2023. URL <https://payloadspace.com/nasa-axes-its-x-57-maxwell-electric-aircraft/>, [Online].

- [9] Brinkmann, P., “X-57 team probes safety question that ended development without a flight,” , July 20 2023. URL <https://aerospaceamerica.aiaa.org/x-57-team-probes-safety-question-that-led-nasa-to-end-development-of-the-electric-aircraft-without-ever-flying-it/#:~:text=NASA%20had%20postponed%20the%20first,subsequent%20design%20fixed%20that%20problem.>, [Online].
- [10] Kim, J., Oh, J., and Lee, H., “Review on battery thermal management system for electric vehicles,” *Applied thermal engineering*, Vol. 149, 2019, pp. 192–212.
- [11] Saw, L. H., Ye, Y., Tay, A. A., Chong, W. T., Kuan, S. H., and Yew, M. C., “Computational fluid dynamic and thermal analysis of Lithium-ion battery pack with air cooling,” *Applied energy*, Vol. 177, 2016, pp. 783–792.
- [12] Sun, H., and Dixon, R., “Development of cooling strategy for an air cooled lithium-ion battery pack,” *Journal of Power Sources*, Vol. 272, 2014, pp. 404–414.
- [13] Singh, S., Jennings, M., Katragadda, S., Che, J., and Miljkovic, N., “System design and analysis methods for optimal electric vehicle thermal management,” *Applied Thermal Engineering*, Vol. 232, 2023, p. 120990.
- [14] Kellermann, H., Fuhrmann, S., Shamiyah, M., and Hornung, M., “Design of a battery cooling system for hybrid electric aircraft,” *Journal of Propulsion and Power*, Vol. 38, No. 5, 2022, pp. 736–751.
- [15] Kellermann, H., Lüdemann, M., Pohl, M., and Hornung, M., “Design and optimization of ram air-based thermal management systems for hybrid-electric aircraft,” *Aerospace*, Vol. 8, No. 1, 2020, p. 3.
- [16] Chapman, J. W., Schnulo, S. L., and Nitzsche, M. P., “Development of a Thermal Management System for Electrified Aircraft,” American Institute of Aeronautics and Astronautics, 2020. <https://doi.org/10.2514/6.2020-0545>.
- [17] Clarke, M., and Alonso, J. J., “Lithium–ion battery modeling for aerospace applications,” *Journal of Aircraft*, Vol. 58, No. 6, 2021, p. 1323–1335.
- [18] Clarke, M. A., and Alonso, J. J., “Forecasting the Operational Lifetime of Battery-Powered Electric Aircraft,” *Journal of Aircraft*, 2022, pp. 1–9. <https://doi.org/10.2514/1.C036851>.
- [19] Bakhti, S., and Dubey, P., “CFD and Experimental Investigation of Graphite Heat Spreader Based Cooling for Li-Ion Batteries for Electric Vehicles and EVTOL (Electric Vertical Take-Off and Landing) Aircraft Applications,” *ASME International Mechanical Engineering Congress and Exposition*, Vol. 86700, American Society of Mechanical Engineers, 2022, p. V008T11A050.
- [20] Zhao, C., Clarke, M., Kellermann, H., and Verstraete, D., “Liquid Cooling Systems for Batteries of Electric Vertical Takeoff and Landing Aircraft,” *Journal of Aircraft*, 2023, pp. 1–17.
- [21] Zhao, C., Mazo, J. R., and Verstraete, D., “Optimisation of a liquid cooling system for eVTOL aircraft: Impact of sizing mission and battery size,” *Applied Thermal Engineering*, Vol. 246, 2024, p. 122988.
- [22] Shekar, S. S., and Clarke, M., “Design and In-Flight Analysis of an Electric Aircraft’s Battery Thermal Management System,” *2024 IEEE Transportation Electrification Conference & Expo (ITEC)*, 2024.
- [23] König, P., Höschler, K., and Haridasu, V. B., “Surface Heat Exchanger Assessment for Battery Powered Aircrafts,” *AIAA AVIATION 2023 Forum*, 2023, p. 4534.
- [24] Laboratory for Electric Aircraft Design and Sustainability, “Research Community Aerospace Interdisciplinary Design Environment,” , June 24 2024. URL <https://github.com/leadsgroup/RCAIDE>, [Online].
- [25] Botero, E. M., Wendorff, A., MacDonald, T., Variyar, A., Vegh, J. M., Lukaczyk, T. W., Alonso, J. J., Orra, T. H., and Ilario da Silva, C., “SUAVE: An Open-Source Environment for Conceptual Vehicle Design and Optimization,” *54th AIAA Aerospace Sciences Meeting*, 2016, pp. 1–16. <https://doi.org/10.2514/6.2016-1275>, URL <http://arc.aiaa.org/doi/10.2514/6.2016-1275>.
- [26] Ukaczyk, T. W., Wendorff, A., Botero, E. M., MacDonald, T., Variyar, A., Vegh, J. M., Alonso, J. J., Orra, T. H., and Ilario da Silva, C., “SUAVE: An Open-Source Environment for Multi-Fidelity Conceptual Vehicle Design,” *54th AIAA Aerospace Sciences Meeting*, 2016, pp. 1–56. <https://doi.org/10.2514/6.2016-1275>, URL <http://arc.aiaa.org/doi/10.2514/6.2016-1275>.
- [27] Vegh, J. M., Botero, E., Clark, M., Smart, J., and Alonso, J. J., “Current Capabilities and Challenges of NDARC and SUAVE for eVTOL Aircraft Design and Analysis,” 2018. <https://doi.org/10.2514/6.2019-4505>, URL <http://arc.aiaa.org>.
- [28] Botero, E. M., Clarke, M. A., Erhard, R. M., Smart, J. T., Alonso, J. J., and Blaufox, A., “Aerodynamic Verification and Validation of SUAVE,” 2022, pp. 1–16. <https://doi.org/10.2514/6.2022-1929>.

- [29] Gallagher, C., Stuart, C., and Spence, S., “Validation and Calibration of Conceptual Design Tool SUAVE,” , No. June, 2023, pp. 1–18. <https://doi.org/10.2514/6.2023-3225>.
- [30] Bergman, T., *Fundamentals of Heat and Mass Transfer*, Wiley, 2011. URL <https://books.google.com/books?id=vvyIoXEywMoC>.
- [31] Kays, W., and London, A., *Compact heat exchangers*, Krieger Pub. Co., 1984. URL <http://books.google.de/books?id=A08qAQAAQAAJ>.
- [32] Virtanen, P., Gommers, R., Oliphant, T. E., Haberland, M., Reddy, T., Cournapeau, D., Burovski, E., Peterson, P., Weckesser, W., Bright, J., van der Walt, S. J., Brett, M., Wilson, J., Millman, K. J., Mayorov, N., Nelson, A. R. J., Jones, E., Kern, R., Larson, E., Carey, C. J., Polat, I., Feng, Y., Moore, E. W., VanderPlas, J., Laxalde, D., Perktold, J., Cimrman, R., Henriksen, I., Quintero, E. A., Harris, C. R., Archibald, A. M., Ribeiro, A. H., Pedregosa, F., van Mulbregt, P., and SciPy 1.0 Contributors, “SciPy 1.0: Fundamental Algorithms for Scientific Computing in Python,” *Nature Methods*, Vol. 17, 2020, pp. 261–272. <https://doi.org/10.1038/s41592-019-0686-2>.
- [33] Hilkevitch, J., “When planes land at O’hare, trip just getting started,” , May 2019. URL <https://www.chicagotribune.com/2015/11/02/when-planes-land-at-ohare-trip-just-getting-started/>.
- [34] Filipe, Anema, F., Story, R., Gardiner, J., Journois, M., Bird, A., Lima, A., Cano, J., dbf, Oefelein, M., Then, H., Baker, J., Leonel, J., Sampson, T., Reades, J., Welsh, B., Rump, H., Fleischmann, M., Kong, Q., Komarov, O., Crosby, A., Harris, G., Dumas, R., KRIEF, D., Furtado, L., kenmatsu4, Nogueira, T. P., and Wilson, N., “python-visualization/folium: v0.17.0,” , Jun 2024. URL <https://zenodo.org/doi/10.5281/zenodo.594439>.